Science Advances
AAAS

Supplementary Materials for

Stable optical lateral forces from inhomogeneities of the spin angular momentum

Yuzhi Shi *et al.*

Corresponding author: Yuzhi Shi, yuzhi_shi01@163.com; Din Ping Tsai, dptsai@cityu.edu.hk; Franco Nori, fnori@riken.jp; Ai Qun Liu, eaqliu@ntu.edu.sg

Sci. Adv. **8**, eabn2291 (2022)
DOI: 10.1126/sciadv.abn2291

This PDF file includes:

Supplementary Notes S1 to S3
Figs. S1 to S14
Table S1

Supplementary Note

Supplementary Note 1: Wave fields

The complex electric field of the plane wave after a quarter-wave plate can be expressed as

$$\mathbf{E} = A\left(\cos\theta\,\overline{\mathbf{x}} + i\sin\theta\,\overline{\mathbf{y}}\right)\exp\left(-ikz\right), \tag{S1}$$

where A is the wave amplitude, $\overline{\mathbf{x}}$ and $\overline{\mathbf{y}}$ are the unit vectors of the corresponding axes, $k = n\omega/c$ is the wavenumber in the medium, $n = \sqrt{\varepsilon\mu}$ is the refractive index of the medium, ω is the frequency, c is the speed of light, and θ is the angle between the electric field of the light beam and the fast axis of the quarter-wave plate, which is also the x-axis. The beam propagates along the $-z$-direction. When θ is 0, $\pi/8$, $\pi/4$ and $3\pi/4$, the light beam is linear, elliptical, left-handed circular and right-handed circular polarizations, respectively.

To investigate the optical lateral force (OLF: force in the y-direction) and eliminate the influence of the optical gradient force, the laser beam is focused by two cylindrical lenses into a line-shaped focal spot with radii w_x and w_y in the x- and y-axes, respectively. In the experiment, we set w_x = 15 μm and w_y = 500 μm, which are much larger than the wavelength of the illuminating light (532 nm), so we can ignore the beam divergence. The electric field of the focused beam can be approximately written as

$$\mathbf{E} = A\left(\cos\theta\,\overline{\mathbf{x}} + i\sin\theta\,\overline{\mathbf{y}}\right)\exp\left[-\left(\frac{x^2}{w_x^2}+\frac{y^2}{w_y^2}\right)\right]\exp\left(-ikz\right). \tag{S2}$$

According to the Maxwell's equation $\nabla\times\mathbf{E} = i\frac{\omega}{c}\mu\mathbf{H}$, where ω is the angular frequency, the magnetic field distribution is given by

$$\mathbf{H} = \frac{Aic}{\omega\mu}\left[\sin\theta k\,\overline{\mathbf{x}} + i\cos\theta k\,\overline{\mathbf{y}} + 2\left(\frac{i\sin\theta x}{w_x^2}-\frac{\cos\theta y}{w_y^2}\right)\overline{\mathbf{z}}\right]\exp\left[-\left(\frac{x^2}{w_x^2}+\frac{y^2}{w_y^2}\right)\right]\exp\left(-ikz\right), \tag{S3}$$

where $\overline{z}$ is the unit vector of the z-axis. The time-average energy density W in a homogenous dielectric medium with permittivity ε and permeability μ is known to be [32, 33, 52]

$$W = W^e + W^m = \frac{g}{2}\left(\varepsilon\left|\mathbf{E}\right|^2 + \mu\left|\mathbf{H}\right|^2\right), \tag{S4}$$

where $g = \left(8\pi\right)^{-1}$ in Gaussian units.

Substituting equations (S2) and (S3) into (S4), we obtain

$$W^e = \frac{g\varepsilon A^2}{2}\exp\left[-2\left(\frac{x^2}{w_x^2}+\frac{y^2}{w_y^2}\right)\right], \tag{S5}$$

$$W^m = \frac{A^2c^2}{\omega^2\mu^2}\left[1+\left(\frac{2\sin\theta x}{w_x^2}\right)^2+\left(\frac{2\cos\theta y}{w_y^2}\right)^2\right]\exp\left[-2\left(\frac{x^2}{w_x^2}+\frac{y^2}{w_y^2}\right)\right]. \tag{S6}$$

The momentum of light $\mathbf{p}$ can be subdivided into the spin momentum $\mathbf{p}_S$ and the canonical (orbital) momentum $\mathbf{p}_O$ as [32, 35, 52]

$$\mathbf{p} = \mathbf{p}_S + \mathbf{p}_O . \tag{S7}$$

In a homogenous non-absorbing medium, they can be described by the following equations with the electric and magnetic contributions [32, 51]:

$$\mathbf{p}_O = \mathbf{p}_O^e + \mathbf{p}_O^m = \frac{g}{2\omega}\mathrm{Im}\left[\frac{1}{\mu}\mathbf{E}^*\cdot(\nabla)\mathbf{E}+\frac{1}{\varepsilon}\mathbf{H}^*\cdot(\nabla)\mathbf{H}\right], \tag{S8}$$

$$\mathbf{p}_S = \mathbf{p}_S^e + \mathbf{p}_S^m = \frac{1}{2}\nabla\times\mathbf{S} = \frac{g}{4\omega}\mathrm{Im}\left[\nabla\times\left(\frac{1}{\mu}\mathbf{E}^*\times\mathbf{E}\right)+\nabla\times\left(\frac{1}{\varepsilon}\mathbf{H}^*\times\mathbf{H}\right)\right], \tag{S9}$$

where $\mathbf{S}$ is the spin angular momentum (SAM), and $\mathbf{C}^*\cdot(\nabla)\mathbf{C}$ is the invariant notation for the vector operation, which can be expressed as [51]

$$\mathbf{C}^*\cdot(\nabla)\mathbf{C} = C_x^*\nabla C_x + C_y^*\nabla C_y + C_z^*\nabla C_z . \tag{S10}$$

Supplementary Note 2: Derivation of the exact equation for the optical lateral force

The total force experienced by a dipolar particle in an electromagnetic field can be expressed as [52]

$$\mathbf{F} = \mathbf{F}_e + \mathbf{F}_m + \mathbf{F}_{em}, \tag{S11}$$

where $\mathbf{F}_e$, $\mathbf{F}_m$ and $\mathbf{F}_{em}$ denote the electric dipole force, the magnetic dipole force and the force from the interference between the electric and magnetic dipoles, respectively. The force originating from an electric dipole is [32, 35]

$$\mathbf{F}_e = \frac{1}{2g\varepsilon}\mathrm{Re}(\alpha_e)\nabla W_e + \frac{\omega\mu}{g}\mathrm{Im}(\alpha_e)\mathbf{p}_O^e, \tag{S12}$$

where α_e is the complex electric polarizability. The first and second terms in equation (S12) correspond to the contributions of the electric part of the inhomogeneous energy distribution (gradient force) and the orbital momentum density, respectively. By substituting equation (S2) into (S4), we obtain $\nabla W_e = 0$, thus the OLF from equation (S12) is

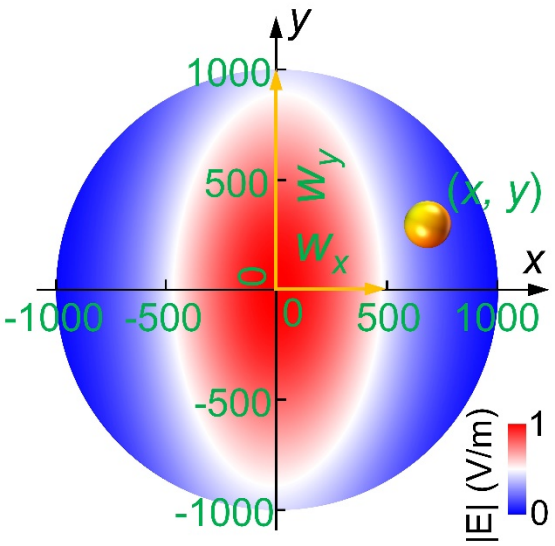

Fig. S1. Illustration of a particle in the simulated line-shaped optical field. The color map represents the simulated electric field of the line-shaped beam. w_x and w_y are the half of the focal widths in the x- and y-directions, respectively. The optical gradient force can be ignored when $w_y \gg \lambda$ (e.g., $w_y = 500$ μm). In the case when $w_y \sim \lambda$, the y-coordinate of the particle is set to 0, to eliminate the optical gradient force in the simulation of the OLF.

$$\mathbf{F}_e^y = \frac{\omega\mu}{g}\mathrm{Im}(\alpha_e)\mathbf{p}_O^e. \tag{S13}$$

In order to eliminate the influence of the optical gradient force, the y-coordinate of the particle is set to be 0 (Fig. S1). Then from equations (S8) and (S10), we obtain

$$\mathbf{p}_O^e = \frac{g}{2\omega\mu}\mathrm{Im}\left(E_x^*\nabla E_x + E_y^*\nabla E_y + E_z^*\nabla E_z\right). \tag{S14}$$

Substituting equation (S14) into equation (S13), $\mathbf{F}_e^y$ can then be expressed as

$$\begin{aligned}\mathbf{F}_e^y &= \frac{1}{2}\mathrm{Im}(\alpha_e)\mathrm{Im}\left(E_x^*\frac{\partial}{\partial y}E_x + E_y^*\frac{\partial}{\partial y}E_y\right)\bar{\mathbf{y}} \\ &= \frac{A}{2}\mathrm{Im}(\alpha_e)\mathrm{Im}\left\{\left[\left(-\frac{2y}{w_y^2}\right)\cdot\left(E_x^*\cdot\cos\theta + E_y^*\cdot i\sin\theta\right)\right]\exp\left[-\left(\frac{x^2}{w_x^2}+\frac{y^2}{w_y^2}\right)\right]\exp(-ikz)\right\}\bar{\mathbf{y}} \\ &= 0\big|_{y=0}.\end{aligned} \tag{S15}$$

The second term of equation (S11) represents the magnetic dipole force, which can be expressed as

$$\mathbf{F}_m = \frac{1}{2g\mu}\mathrm{Re}\left(\alpha_m\right)\nabla W_m + \frac{\omega\varepsilon}{g}\mathrm{Im}\left(\alpha_m\right)\mathbf{p}_O^m, \tag{S16}$$

where α_m is the complex magnetic polarizability. Similar to $\mathbf{F}_e$, the first term of equation (S16) also corresponds to the gradient force, and is zero due to the *y*-related term in the chosen coordinate system, while the second term of equation (S16) is not zero. The magnetic dipole related OLF can be derived under the conditions, $y = 0$ and $z = 0$ to be

$$\begin{aligned}\mathbf{F}_m^y &= \frac{\omega\varepsilon}{g}\mathrm{Im}\left(\alpha_m\right)\mathbf{p}_O^m \\ &= \frac{1}{2}\mathrm{Im}\left(\alpha_m\right)\mathrm{Im}\left(H_x^*\frac{\partial}{\partial y}H_x + H_y^*\frac{\partial}{\partial y}H_y + H_z^*\frac{\partial}{\partial y}H_z\right)\overline{\mathbf{y}} \\ &= \frac{2A^2c^2\sin\theta\cos\theta x}{\omega^2\mu^2 w_x^2 w_y^2}\mathrm{Im}\left(\alpha_m\right)\exp\left(-\frac{2x^2}{w_x^2}\right)\overline{\mathbf{y}}\Big|_{y=0;z=0}.\end{aligned} \tag{S17}$$

Here, we see that, in sharp contrast to $\mathbf{F}_e^y = 0$, $\mathbf{F}_m^y \neq 0$ when $\mathrm{Im}\left(\alpha_m\right) \neq 0$. This phenomenon is due to the non-zero orbital momentum density caused by $H_Z \neq 0$. $\mathbf{F}_e^y = \mathbf{F}_m^y = 0$ for a plane wave.

Next, we investigate the force $\mathbf{F}_{em}$ originating from the interference between electric and magnetic dipoles, which can be expressed as [15, 52]

$$\mathbf{F}_{em} = -\frac{\omega}{3g}k^3\,\mathrm{Re}\left(\alpha_e\alpha_m^*\right)\left(\mathbf{p}_S + \mathbf{p}_O\right) - \frac{\omega}{3c}k^3\,\mathrm{Im}\left(\alpha_e\alpha_m^*\right)\mathrm{Im}\left(\mathbf{E}^*\times\mathbf{H}\right). \tag{S18}$$

Here, the complex electric polarizability α_e determining the electric dipole moment $\mathbf{d}_e$ induced by the electric field $\mathbf{E}$ and the magnetic polarizability α_m determining the magnetic dipole moment $\mathbf{d}_m$ induced by the magnetic field $\mathbf{H}$ are defined via equations $\mathbf{d}_e = \alpha_e\mathbf{E}$ and $\mathbf{d}_m = \mu^{-1}\alpha_m\mathbf{H}$, respectively. The complex electric polarizability α_e can be written as

$$\alpha_e = \alpha_e^0\left(1 - i\frac{2}{3\varepsilon}k^3\alpha_e^0\right)^{-1}, \tag{S19}$$

with

$$\alpha_e^0 = \varepsilon a^3\frac{\varepsilon_p - \varepsilon}{\varepsilon_p + 2\varepsilon} = \varepsilon a^3 B_e, \tag{S20}$$

where a and ε_p are the radius and permittivity of the particle, and $B_e = \dfrac{\varepsilon_p - \varepsilon}{\varepsilon_p + 2\varepsilon}$. Therefore,

$$\alpha_e = \frac{9\varepsilon a^3 B_e + i6\varepsilon k^3 a^6 B_e^2}{9 + 4k^6 a^6 B_e^2}. \tag{S21}$$

Similarly, the magnetic polarizability can be expressed as

$$\alpha_m = \alpha_m^0 \left(1 - i\frac{2}{3\mu} k^3 \alpha_m^0\right)^{-1}, \tag{S22}$$

with

$$\alpha_m^0 = \mu a^3 \frac{\mu_p - \mu}{\mu_p + 2\mu} = \mu a^3 B_m, \tag{S23}$$

where μ_p is the permeability of the particle, and $B_m = \frac{\mu_p - \mu}{\mu_p + 2\mu}$. Therefore,

$$\alpha_m = \frac{3\mu a^3 B_m \left(3 + 2ik^3 a^3 B_m\right)}{9 + 4k^6 a^6 B_m^2}. \tag{S24}$$

Considering a non-magnetic polystyrene dipolar particle (radius a = 10 nm, relative permittivity $\varepsilon_p = 2.4336$ and permeability $\mu_p = 1$) in a homogeneous environment ($\varepsilon = 2.1316$, $\mu = 1$), $B_e = 0.0451$ and $B_m = 0$ can be obtained. Subsequently,

$$\mathrm{Im}(\alpha_m) = \frac{6\mu k^3 a^6 B_m^2}{9 + 4k^6 a^6 B_m^2} = 0, \tag{S25}$$

$$\mathbf{F}_m = 0. \tag{S26}$$

Thus, both the electric and magnetic dipolar forces are absent in the considered geometry. The electric dipolar force equals zero because of the gradient-symmetry and the absence of the electric orbital momentum. The magnetic dipole force equals zero due to the zero magnetic polarizability even in the presence of the magnetic orbital momentum. Overall, the contributions from the optical gradient force and orbital energy flow are zero for non-magnetic dipolar particles. Besides, the force from the interference between the electric and magnetic dipole radiation [equation (S18)] is also zero because $\alpha_e^* \alpha_m = 0$. The OLF on an ideal non-magnetic dipole particle is absent under the conditions considered.

Nevertheless, when the particle is not an ideal dipolar particle (i.e., $a \sim \lambda$), the electric and magnetic polarizabilities of a spherical particle can be obtained from the Mie scattering coefficients [35, 63]

$$\alpha_e = \frac{\varepsilon}{k^3}\left\{\frac{\varepsilon_p - \varepsilon}{\varepsilon_p + 2\varepsilon}(ka)^3 + \frac{3}{10}\frac{\varepsilon_p^2 + \varepsilon_p\varepsilon\left[\left(\varepsilon_p\mu_p / \varepsilon\mu\right) - 6\right] + 4\varepsilon^2}{\left(\varepsilon_p + 2\varepsilon\right)^2}(ka)^5\right\}, \tag{S27}$$

$$\alpha_m = \frac{\mu}{k^3}\left\{\frac{\mu_p - \mu}{\mu_p + 2\mu}(ka)^3 + \frac{3}{10}\frac{\mu_p^2 + \mu_p\mu\left[\left(\varepsilon_p\mu_p / \varepsilon\mu\right) - 6\right] + 4\mu^2}{\left(\mu_p + 2\mu\right)^2}(ka)^5\right\}. \tag{S28}$$

For a non-magnetic nanoparticle and the surrounding medium, $\mu_p = \mu = 1$, which results in

$$\alpha_e \cong \varepsilon a^3 \frac{\varepsilon_p - \varepsilon}{\varepsilon_p + 2\varepsilon}, \tag{S29}$$

$$\alpha_m = k^2 a^5 \frac{\varepsilon_p - \varepsilon}{30\varepsilon}. \tag{S30}$$

Consequently,

$$\mathrm{Re}\left(\alpha_e\alpha_m^*\right) \cong \frac{k^2a^8}{30}\left|\frac{\varepsilon_p - \varepsilon}{\varepsilon_p + 2\varepsilon}\right|^2\left[\mathrm{Re}\left(\varepsilon_p\right) + 2\right], \tag{S31}$$

$$\mathrm{Im}\left(\alpha_e\alpha_m^*\right) \cong -\frac{k^2a^8}{30}\left|\frac{\varepsilon_p - \varepsilon}{\varepsilon_p + 2\varepsilon}\right|^2\mathrm{Im}\left(\varepsilon_p\right). \tag{S32}$$

Equation (S32) applies when $\mathrm{Im}(\varepsilon) = 0$. To investigate $\mathbf{F}_{em}$, we substitute equation (S2) into the first term of equation (S9):

$$\begin{aligned}
\mathbf{p}_S^e &= \frac{g}{4\omega\mu}\mathrm{Im}\nabla\times\left(\mathbf{E}^*\times\mathbf{E}\right) \\
&= \frac{g}{4\omega\mu}\mathrm{Im}\nabla\times\left\{\left(\cos\theta\,\overline{\mathbf{x}} - i\sin\theta\,\overline{\mathbf{y}}\right)\times\left(\cos\theta\,\overline{\mathbf{x}} + i\sin\theta\,\overline{\mathbf{y}}\right)\cdot\exp\left[-2\left(\frac{x^2}{w_x^2} + \frac{y^2}{w_y^2}\right)\right]\right\}\Bigg|_{z=0} \\
&= \frac{g}{2\omega\mu}\mathrm{Im}\nabla\times\left\{\cos\theta\sin\theta\exp\left[-2\left(\frac{x^2}{w_x^2} + \frac{y^2}{w_y^2}\right)\right]\overline{\mathbf{z}}\right\}\Bigg|_{z=0} \\
&= \frac{2g\cos\theta\sin\theta}{\omega\mu}\exp\left[-2\left(\frac{x^2}{w_x^2} + \frac{y^2}{w_y^2}\right)\right]\mathrm{Im}\left(-\frac{y}{w_y^2}\,\overline{\mathbf{x}} + \frac{x}{w_x^2}\,\overline{\mathbf{y}}\right)\Bigg|_{z=0} \\
&= 0.
\end{aligned} \tag{S33}$$

Similarly, substituting equation (S2) into the second term of equation (S9):

$$\begin{aligned}\mathbf{p}_S^{m,y} &= \frac{g}{4\omega\varepsilon}\mathrm{Im}\nabla\times\left(\mathbf{H}^*\times\mathbf{H}\right)\\ &= \frac{gc^2A^2}{4\varepsilon\mu^2\omega^3}\mathrm{Im}\nabla\times\left\{\left(\frac{4ik\cos^2\theta y}{w_y^2}\overline{\mathbf{x}}-\frac{4ik\sin^2\theta x}{w_x^2}\overline{\mathbf{y}}+2ik^2\cos\theta\sin\theta\,\overline{\mathbf{z}}\right)\cdot\exp\left[-2\left(\frac{x^2}{w_x^2}+\frac{y^2}{w_y^2}\right)\right]\right\}\Bigg|_{z=0}\\ &= \frac{2gk^2c^2A^2\cos\theta\sin\theta x}{\varepsilon\mu^2\omega^3w_x^2}\exp\left(-\frac{2x^2}{w_x^2}\right)\overline{\mathbf{y}}\Big|_{y=0;z=0},\end{aligned} \tag{S34}$$

with $\mathbf{p}_S^{m,y}$ denoting the spin momentum component in the *y*-direction.

Meanwhile,

$$\begin{aligned}\mathbf{p}_O^m &= \frac{g}{2\omega\varepsilon}\mathrm{Im}\left(H_x^*\frac{\partial}{\partial y}H_x+H_y^*\frac{\partial}{\partial y}H_y+H_z^*\frac{\partial}{\partial y}H_z\right)\overline{\mathbf{y}}\\ &= \frac{g}{2\omega\varepsilon}\mathrm{Im}\left(0+0+H_z^*\frac{\partial}{\partial y}H_z\right)\overline{\mathbf{y}}\Big|_{y=0;z=0}\\ &= \frac{2A^2c^2\,\mathrm{g}\cos\theta\sin\theta x}{\omega^3\varepsilon\mu^2w_x^2w_y^2}\exp\left(-\frac{2x^2}{w_x^2}\right)\overline{\mathbf{y}}\Big|_{y=0;z=0}.\end{aligned} \tag{S35}$$

The last term of equation (S18), which is also the Poynting vector (**P**)-related term can be derived as

$$\begin{aligned}\mathrm{Im}\left(\mathbf{P}\right)^y &= \mathrm{Im}\left(\frac{2A^2c\cos\theta\sin\theta x}{\omega\mu w_x^2}\exp\left(-\frac{2x^2}{w_x^2}\right)\Big|_{y=0;z=0}\right)\overline{\mathbf{y}}\\ &= 0.\end{aligned} \tag{S36}$$

Combining the derived OLF contributions by substituting equations (S34) and (S35) into equation (S18), the exact expression for the OLF on a non-absorbing particle can be obtained:

$$\begin{aligned}\mathbf{F}_{\mathrm{OLF}}\left(x,0\right) &= -\frac{\omega}{3g}k^3\,\mathrm{Re}\left(\alpha_e\alpha_m^*\right)\left(\mathbf{p}_S^m+\mathbf{p}_o^m\right)\\ &= -\frac{2k^3c^2A^2\cos\theta\sin\theta x}{3\varepsilon\mu^2\omega^2w_x^2}\mathrm{Re}\left(\alpha_e\alpha_m^*\right)\left(k^2+\frac{1}{w_y^2}\right)\exp\left(-\frac{2x^2}{w_x^2}\right)\overline{\mathbf{y}}.\end{aligned} \tag{S37}$$

Equation (S37) can also be obtained using equation (44) in Ref. [52], whose first term is proportional to the real part of the Poynting vector [$\mathrm{Re}\left(\mathbf{P}\right)$]. Note that $\mathrm{Re}\left(\mathbf{P}\right)$ can be divided into the sum of the spin and orbital momentum densities

$$\mathrm{Re}\left(\mathbf{P}\right)\propto\left(\mathbf{p}_S+\mathbf{p}_O\right). \tag{S38}$$

Then equation (44) in Ref. [52] can be easily converted to equation (S18).

The OLF on an absorbing particle also has contributions from the magnetic dipole force, and the explicit expression can be obtained by combining equations (S17) and (S37) as

$$\begin{aligned}\mathbf{F}_{\mathrm{OLF}}(x,0)=\mathbf{F}_m+\mathbf{F}_{em}&=\frac{\omega}{g}\left[\varepsilon\,\mathrm{Im}(\alpha_m)\mathbf{p}_O^m-\frac{k^3}{3}\mathrm{Re}\left(\alpha_e\alpha_m^*\right)\left(\mathbf{p}_S^m+\mathbf{p}_o^m\right)\right]\\&=\frac{2A^2c^2\sin\theta\cos\theta x}{\omega^2\mu^2w_x^2w_y^2}\left[\mathrm{Im}(\alpha_m)-\frac{k^3w_y^2}{3\varepsilon}\mathrm{Re}\left(\alpha_e\alpha_m^*\right)\left(k^2+\frac{1}{w_y^2}\right)\right]\exp\left(-\frac{2x^2}{w_x^2}\right)\bar{\mathbf{y}}.\end{aligned}\tag{S39}$$

It is worth noting that, $k^2 \gg w_y^2$ when $w_y \gg \lambda$. Thus, the OLF is in the opposite direction of $\mathbf{p}_S^m$ for a non-absorbing particle since $\mathrm{Re}\left(\alpha_e\alpha_m^*\right)>0$ and $\mathrm{Im}(\alpha_m)=0$. Whereas $\mathbf{F}_{em}$ in the OLF can be in a same direction of $\mathbf{p}_S^m$ for a metallic particle when $\mathrm{Re}(\varepsilon_p)+2<0$ [see equation (S31)]. Meanwhile, $\mathbf{F}_m$ in the OLF also emerges because $\mathrm{Im}(\alpha_m)\neq 0$. Thus, the OLF on a metallic particle can be larger than that on a non-absorbing particle.

Equation (S39) is the equation of the OLF in the main text [equation (3)]. It should be noted that equation (S39) is implemented in Gaussian units, it can be easily converted to SI units. The quantitative dependences of the OLF on the polarization of the incident light and particle position are shown in Fig. S2. The OLF has maximum values and opposite signs for the left and right-handed circularly polarized incident light. The sign of the OLF reverses when the particle is placed on different sides with respect to the axis, $x = 0$.

Similarly, the spin-dependent force in the x-direction when the particle is placed at $x = 0$ can be obtained as

$$\begin{aligned}\mathbf{F}_{\mathrm{OLF}}(y,0)=\mathbf{F}_m+\mathbf{F}_{em}&=\frac{\omega}{g}\left[\varepsilon\,\mathrm{Im}(\alpha_m)\mathbf{p}_O^m-\frac{k^3}{3}\mathrm{Re}\left(\alpha_e\alpha_m^*\right)\left(\mathbf{p}_S^m+\mathbf{p}_o^m\right)\right]\\&=\frac{2A^2c^2\sin\theta\cos\theta y}{\mu^2\omega^2w_x^2w_y^2}\left[\mathrm{Im}(\alpha_m)-\frac{k^3w_x^2}{3\varepsilon}\mathrm{Re}\left(\alpha_e\alpha_m^*\right)\left(k^2+\frac{1}{w_x^2}\right)\right]\exp\left(-\frac{2y^2}{w_y^2}\right)\bar{\mathbf{x}}.\end{aligned}\tag{S40}$$

It is noted that this spin-dependent force in the x-direction is much smaller than that in the y-direction because $w_y \gg w_x$. Meanwhile, the gradient force in the x-direction can be larger than the negligible spin-dependent force in the y-direction (Fig. 2A). Therefore, the optical gradient force and the radiation pressure force are the two dominant forces in the x-direction, as shown in Fig. 4A. In contrast, the optical gradient force in the y-direction is largely diminished by choosing w_y = 500 μm, facilitating the investigation of the OLF in the y-direction.

Supplementary Note 3: Simulation of the Brownian motion of particle

For a particle in a force field, the kinetics of the particle can be expressed using the Langevin equation [5, 61]

$$m\frac{d^2}{dt^2}r(t) = -\gamma\frac{d}{dt}r(t) + F(r) + \chi(t), \tag{S41}$$

where m is the mass of the particle, r is the particle position, $F(r)$ is the external force field, γ is the particle friction coefficient, which for a spherical particle of radius a moving in a fluid with a viscosity η, can be determined by Stokes' law as $\gamma = 6\pi\eta a$. And $\chi(t)$ is the random force with zero mean, which can be written as $\chi(t) = \sqrt{2S}W(t)$, where $W(t)$ is a white noise with $\langle W(t)\rangle = 0$, and $2S$ is the intensity of the noise. In the low Reynolds number regime, the overdamped Langevin equation can be obtained by omitting the inertial term as

$$\gamma\frac{d}{dt}r(t) = F(r) + \xi(t), \tag{S42}$$

where $\xi(t) = \sqrt{2D}W(t)$ is a white noise with intensity 2D, where $D = k_B T/\gamma$ is the diffusion coefficient. Here, k_B is the Boltzmann constant, and T is the temperature.

In the two-dimensional force field shown in Fig. 4A, apart from the Brownian motion, the particle experiences the optical gradient force with a spring constant k_x and the optical radiation pressure force F_{rad} in the x-direction, while only the OLF in the y-direction. Using the two-dimensional Langevin equation, we obtain

$$\begin{cases} \dfrac{dx(t)}{dt} = \dfrac{F_{\text{rad}} - k_x x(t)}{\gamma} + \sqrt{2D}W_x(t) \\ \dfrac{dy(t)}{dt} = \dfrac{F_{\text{OLF}}(x)}{\gamma} + \sqrt{2D}W_y(t). \end{cases} \tag{S43}$$

We then simulate the particle trajectories in this force field. For simplicity, k_x is set to 2×10^{-8} N/m, and F_{rad} is set to 100 fN. F_{OLF} is set to $30\frac{x}{|x|}$ fN, which means that the OLFs are negative and positive on the left ($x < 0$) and right ($x > 0$) sides of the beam, respectively, mimicking the OLF in the right-handed circularly polarized beam. The initial position of the particle is set to (−10 μm, 0). The time ranges in the simulation are set to 10 and 100 s. The OLF is chosen to be slightly larger than that measured in the experiment (Fig. 5A), to better mimic the practical situation, where the measured force is weaker due to the friction between the particle and substrate. The simulation results of two-dimensional particle trajectories are shown in Fig. S3.

As we can see from Fig. S3, the particle moves downward on the left of the beam, while moving upward after crossing the beam center at $x = 0$. The trajectory matches relatively well with the experimental results in Fig. 4E.

The Brownian motion makes a significant impact on the particle trajectory, as shown in Fig. S3. In a short range of time, i.e., a few seconds, the particle may move in the opposite direction of the OLF, which is also reflected in the experimental trajectories in Fig. 4 (C-F). Meanwhile, the oscillation range of the Brownian motion can reach 1-2 μm, which also matches that in the experiment. We also investigate the effect of liquid viscosity on the kinetics of particles, as shown in Fig. S4. Since the diffusion coefficient is inversely proportional to the viscosity, the Brownian motion is more prominent in a low-viscosity liquid than that in a high-viscosity liquid. The Brownian motion may overwhelm the OLF because both of them could move the particle in the same dimension (Fig. S4C), causing difficulties in observing the bidirectional movements of particle in the *y*-direction on both sides of the beam. Meanwhile, the particle will be quickly pushed to the stable position in the *x*-direction (Fig. 4A), and the observation time for the bidirectional movement of the particle will be short. The most important reason why (low-viscosity) water is not suitable for the experiment is that the refractive index of water is 1.33, which is different from that of quartz (substrate), resulting in an inhomogeneous environment for the particle.

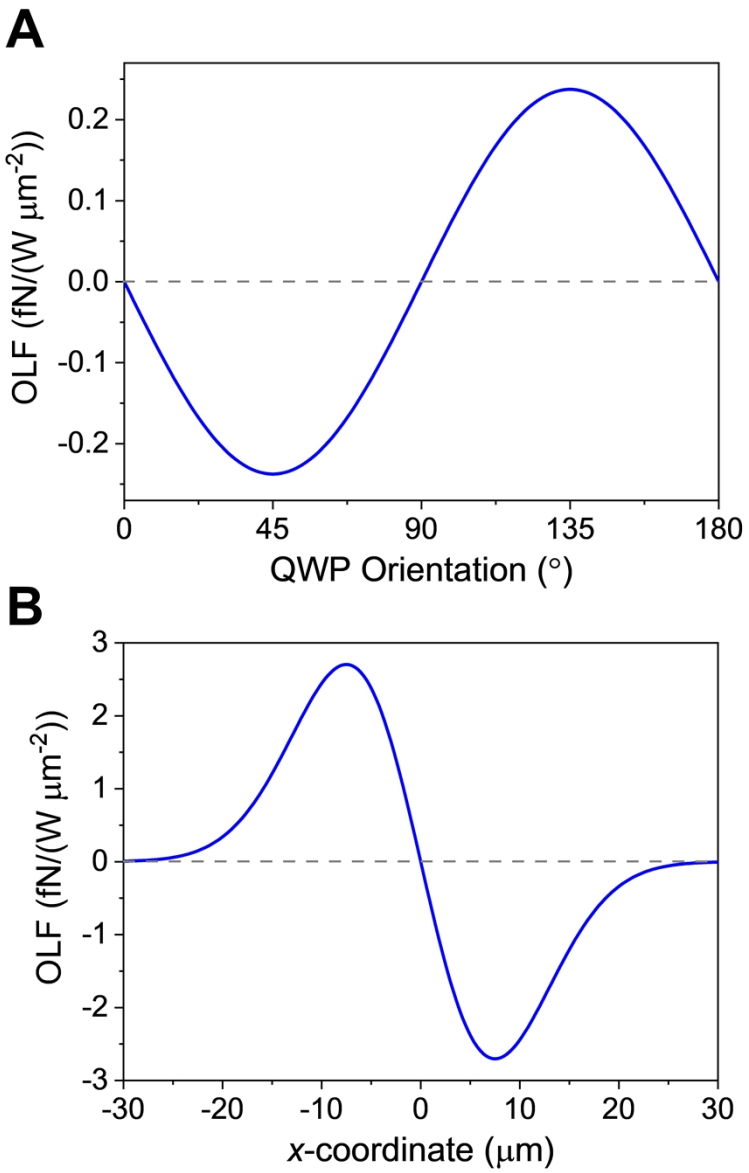

Fig. S2. Optical lateral force calculated using equation (S39). a, The dependence of the OLF on the polarization of the incident light (orientation of the quarter-wave plate). The OLF reaches its maximum values at $\theta = 45°$ and 135°, corresponding to the left and right-handed circular polarizations. The particle position is ($x = 400$ nm, $y = 0$), as shown in Fig. S1. **b**, Optical lateral force at different locations along the x-axis for $\theta = 45°$. The sign of the OLF reverses after crossing the center of the beam ($x = 0$). Simulation parameters are $w_x = 15$ μm, $w_y = 500$ μm, $\varepsilon = (1.46)^2$, $\varepsilon_p = (1.56)^2$, and $a = 25$ nm. The OLFs in **a** and **b** are calculated by normalizing the intensity at ($x = 0$, $y = 0$) to 1 W/μm^2, where it is highest.

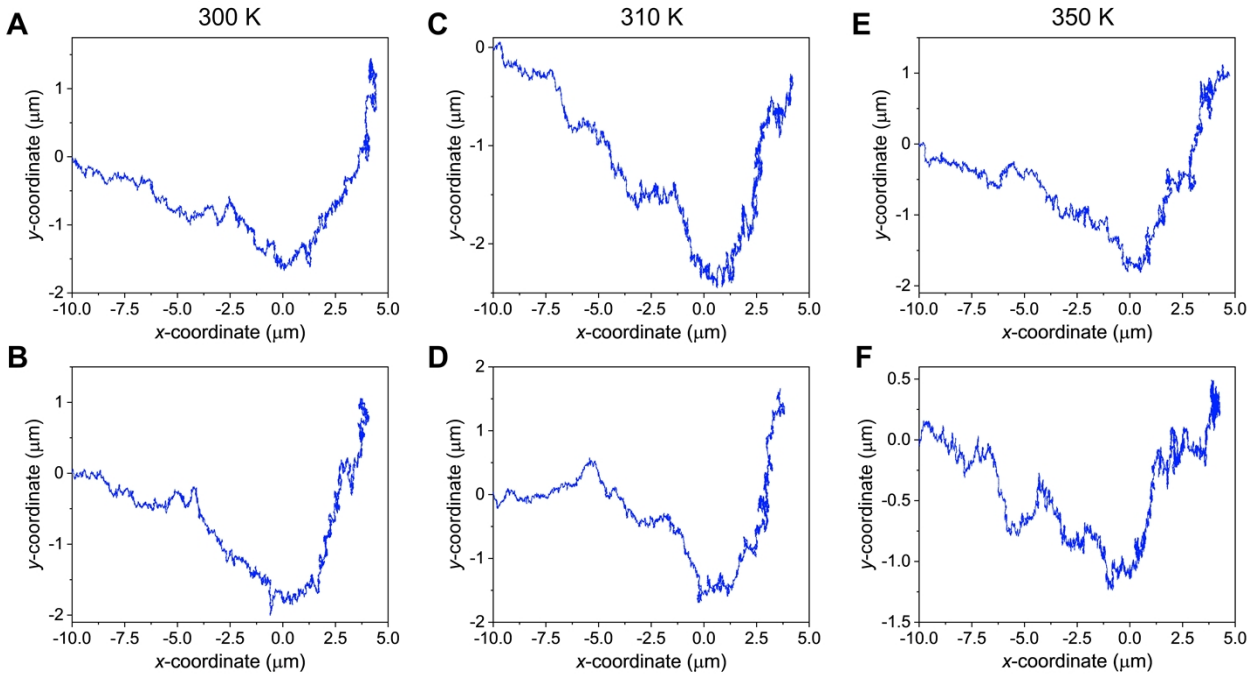

Fig. S3. Simulated trajectories of 5-μm-diameter particles with the Brownian motion in the two-dimensional force field. a,**b**, $T = 300$ K. **c**,**d**, $T = 310$ K. **e**,**f**, $T = 350$ K. The beam center is at $x = 0$. The particle experiences the optical gradient force in the x-direction with the spring constant $k_x = 2\times10^{-8}$ N/m, the radiation pressure force $F_{\mathrm{rad}} = 100$ fN, the OLF $= 30\frac{x}{|x|}$ fN. The particle may move in the opposite direction of the OLF in a short range of time, which is also reflected in the experimental trajectories in Fig. 4 (C-F) in the main text. **a** and **b**, **c** and **d**, **e** and **f** are simulated under the same parameters, they have different trajectories because the Brownian motion is random.

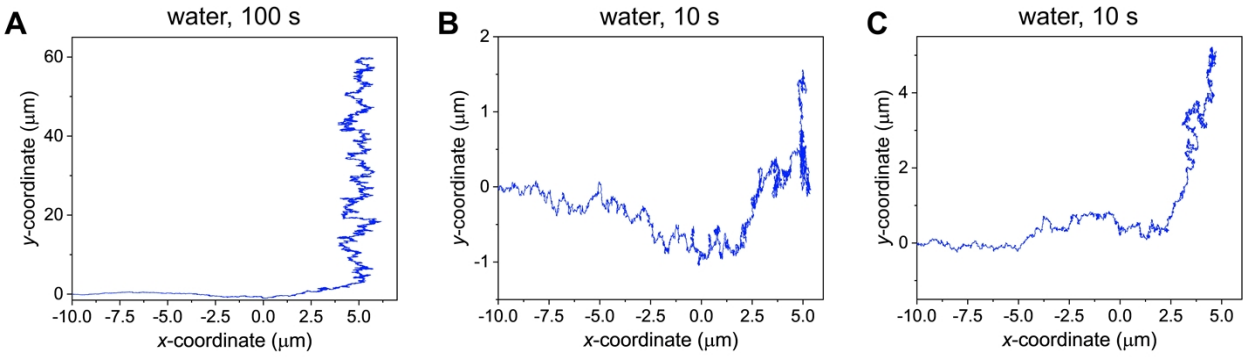

Fig. S4. Simulated trajectories of 5-μm-diameter particles inside water. a, The trajectory of the particle in water in a time range of 100 s. **b**,**c**, The trajectories of particles in water in a time range of 10 s. The low-viscosity water results in a larger diffusion coefficient *D* and faster movement of the particle, causing difficulties in observing the bidirectional movement of particle on both sides of the beam. Most importantly, the refractive index of water (RI = 1.33) does not match the quartz substrate (RI = 1.46), resulting in an inhomogeneous environment for the particle. The simulation parameters are the same in Fig. S3.

Additional Figures

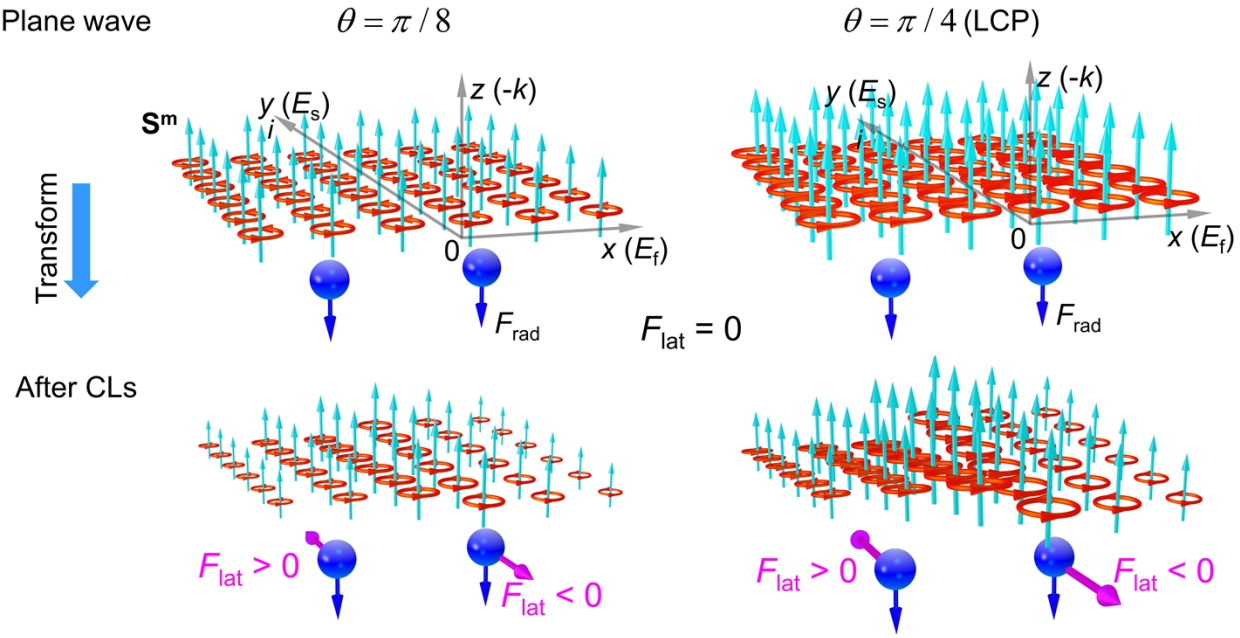

Fig. S5. Helicity-dependent magnetic SAM $\mathbf{S}^m$ and optical forces with different orientation angles of the quarter-wave plate. The distribution of $\mathbf{S}^m$ before focusing by two cylindrical lenses (CLs) is homogeneous for $\theta = 22.5°$ and 45°. $\mathbf{S}^m$ has the same direction for both angles. The corresponding OLFs for both angles after focusing by two CLs dominantly point along the $+y$ and $-y$ directions at the regions $x < 0$ and $x > 0$, respectively. The $\mathbf{S}^m$ and the OLF for $\theta = 22.5°$ are both smaller than those for $\theta = 45°$.

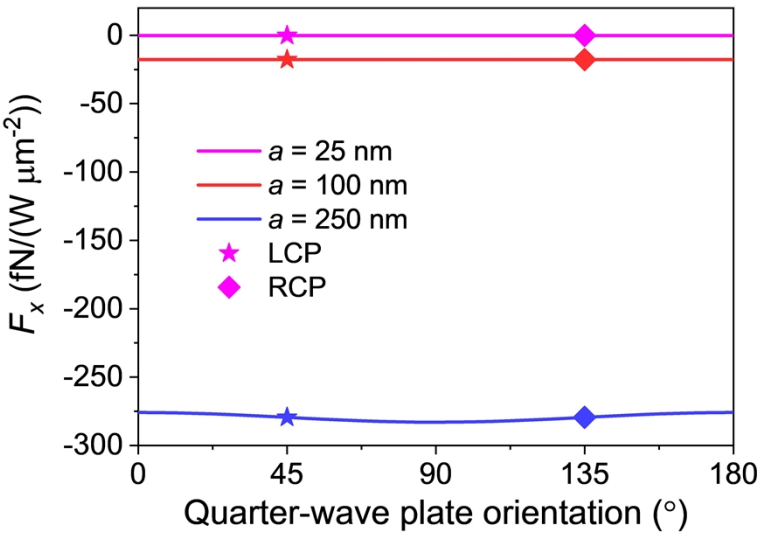

Fig. S6. Dependence of the optical force in the *x*-direction on the polarizations of the incident light. The force increases significantly with the particle size. All particles are placed at x = 700 nm. Here, $\varepsilon = (1.46)^2$, $\varepsilon_p = (1.56)^2$, $\mu = \mu_p = 1$, w_x = 15 μm, w_y = 500 μm. In contrast to the OLF dependence, F_x remains almost constant and negative for all polarizations, acting toward the beam center ($x = 0$). The forces are calculated by normalizing the intensity at ($x = 0$, $y = 0$) to 1 W/μm^2, where it is highest.

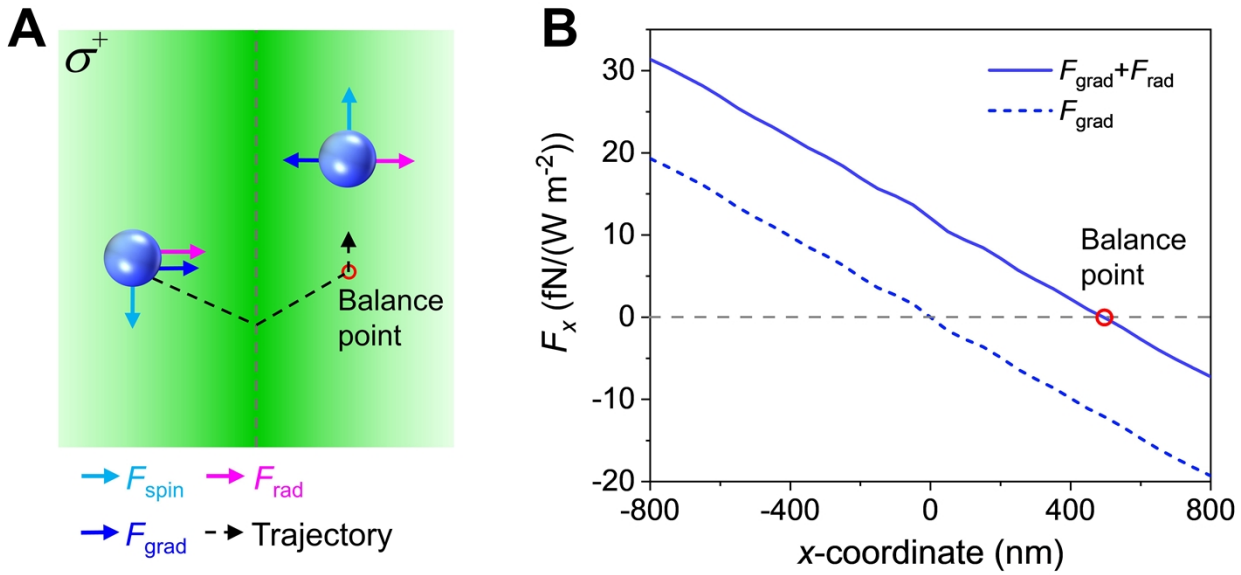

Fig. S7. Particle dynamics in the line-shaped beam under the illumination of the right-handed circularly polarized (RCP) beam. a, Illustration of a particle with a radius of 100 nm moving in a line-shaped beam: the particle on the left of the beam moves toward the +x direction by the optical radiation pressure force F_{rad} and the optical gradient force F_{grad}. It eventually stops moving in the x-direction by the balance of the F_{rad} and F_{grad} on the right side of the beam. The particle moves downward and rightward in the y-direction by the OLF. **b**, Calculations of optical forces in the x-direction. The balance point is located at $x = 0$ without F_{rad}. It shifts to the right side of the beam under the balance of F_{grad} and F_{rad} when the beam is obliquely incident. The simulation parameters are w_x = 15 μm, w_y = 500 μm, and a = 100 nm. The optical forces are calculated by normalizing the intensity at ($x = 0$, $y = 0$) to 1 W/μm^2, where it is highest.

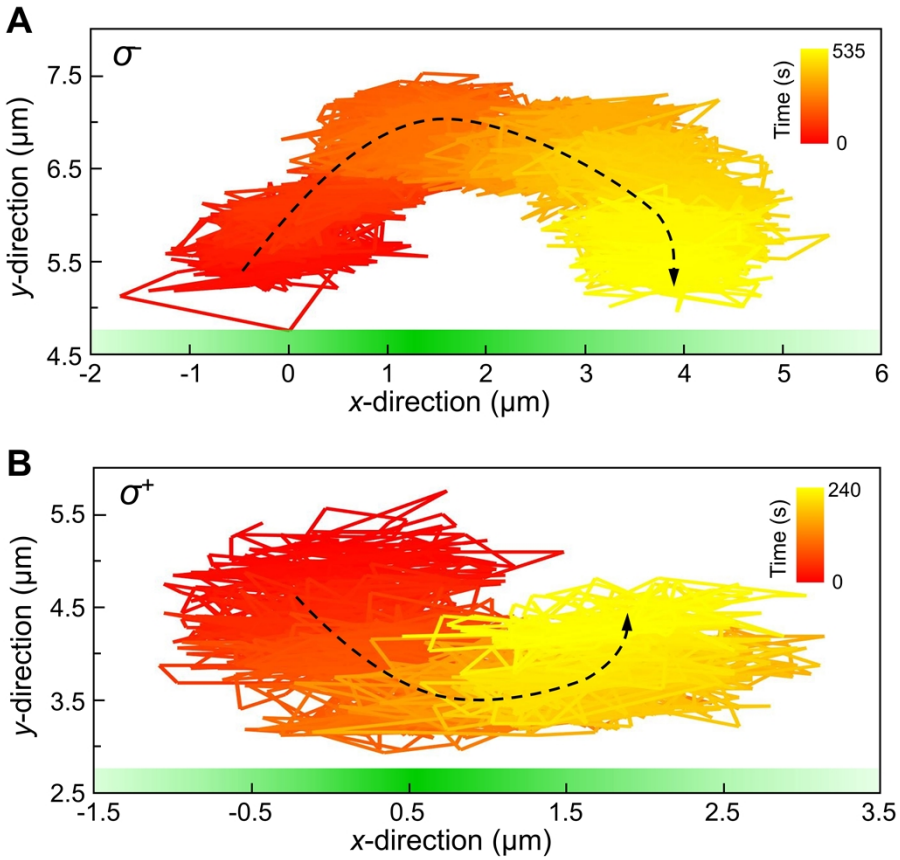

Fig. S8. 2D Time-dependent position of particles in Scenario 1. a, Experimental trajectory shows that the particle moves from top to bottom in the *y*-direction when crossing the beam center ($x = 0$) for the LCP light. The particle moves toward the $+x$-direction until reaching the balance point of the optical radiation pressure force and optical gradient force. **b,** Experimental trajectory shows that the particle moves from bottom to top in the *y*-direction when crossing the beam center for the RCP light.

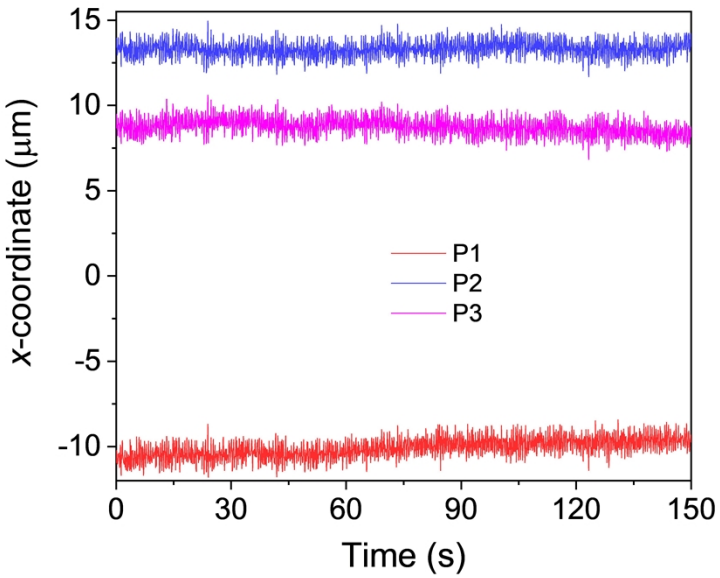

Fig. S9. Time-dependent positions of particles P1, P2 and P3 (shown in Fig. 4, C and F) in the *x*-direction. The optical gradient force and radiation pressure force push P1 along the +*x*-direction, while the gradient forces on P2 and P3 move them slowly in the −*x*-direction. Consequently, the displacement of P1 (due to the optical gradient force plus the radiation pressure force) is more prominent than P2 and P3 (due to the optical gradient force minus the radiation pressure force).

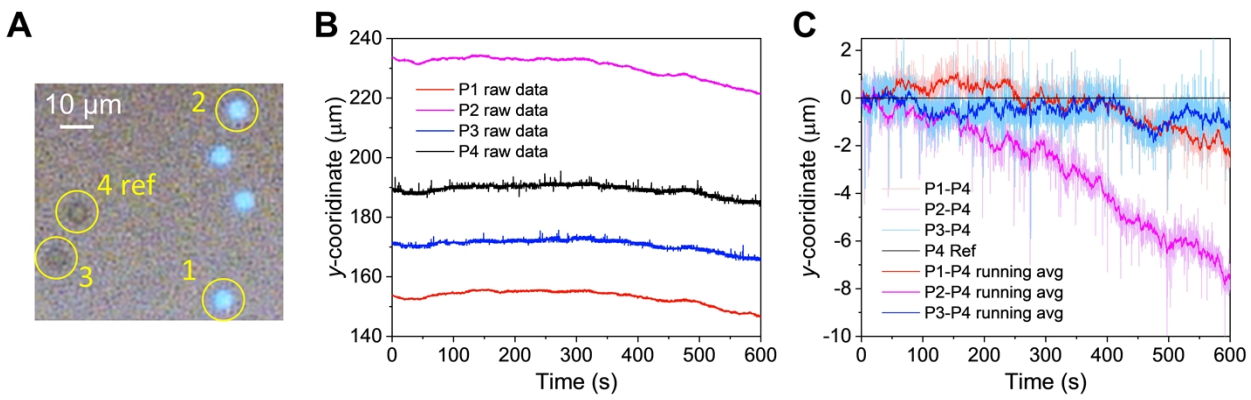

Fig. S10. Time-dependent positions of particles in a long-time range. a, Image of particles. Particles [e.g., Particle 1 (P1) and P2] in the laser beam look brighter than those outside the laser beam (i.e., P3 and P4). Because in a long-time range (10 min), there occurs an inevitable background drifting, which should be considered; P4 is used as the reference particle. Though the background drift can be very small and ignored in previous particle trapping scenarios, it can be a prominent effect in this work because the OLF is small and can be affected by any factor. **b**, Raw data of trajectories of P1-P4 in the *y*-direction. As can been seen, P3 and P4 have a similar trajectory, which affects the moving of P1 and P4. **c**, Trajectories of P1-P4 in the *y*-direction after subtracting that of P4. It is clearly seen that P2 moves toward the −*y*-direction, P1 moves up and down when crossing the center of the beam, P3 moves randomly due to the Brownian motion. It is also worth noting that, vibrations, such as the vibration of camera or the optical stage, may also contribute to the noise in the curves, but they imposed on all particles and are not random, and, therefore, do not influence the observation of the OLF. The beam is left-handed circularly polarized beam with a power of 800 mW.

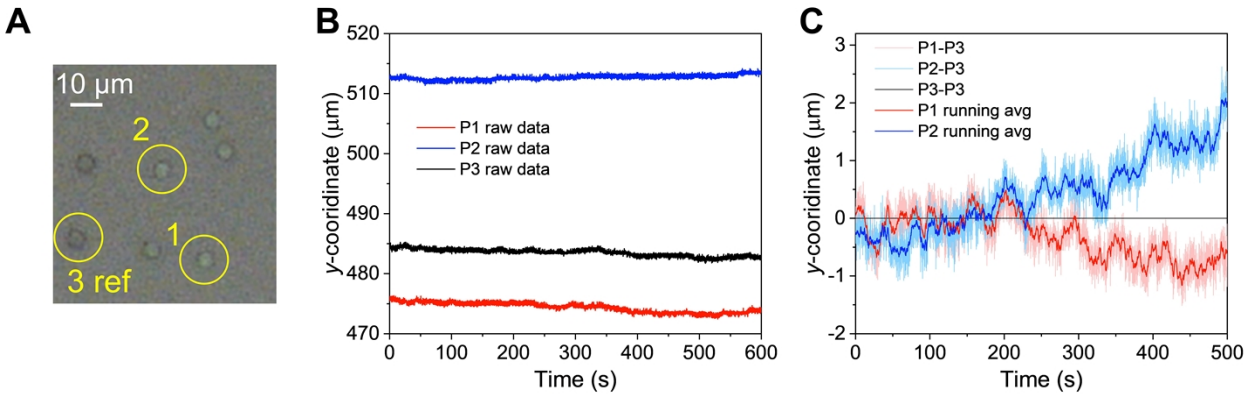

Fig. S11. Bidirectional motion of particles on two sides of the beam in a long-time range. a, Image of particles. P1 and P2 are on the right and left sides of the beam, respectively. P4 is used as the reference particle. **b**, Raw data of trajectories of P1-P3 in the *y*-direction. **c**, Trajectories of P1-P3 in the *y*-direction after subtracting that of P3. It is clearly seen that P1 moves toward the −*y*-direction, while P2 moves toward the +*y*-direction. The beam is left-handed circularly polarized beam with a power of 800 mW.

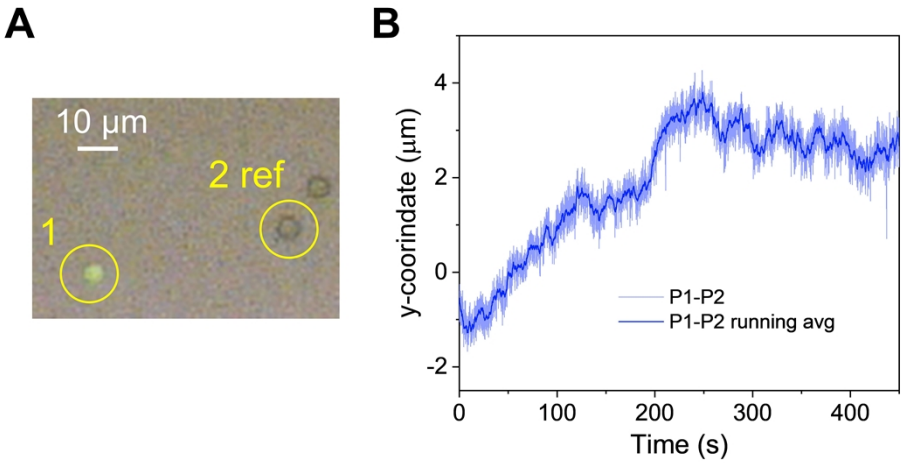

Fig. S12. The trajectory of a particle in the *y*-direction when crossing the beam center. a, Image of particles. P1 is initially on the left side of the beam and moves to the right side. P2 is used as the reference particle. **b**, Trajectory of a particle (P1) in the *y*-direction after subtracting that of P2. P1 moves up and down before and after crossing the beam center, respectively. The beam is left-handed circularly polarized beam with a power of 900 mW.

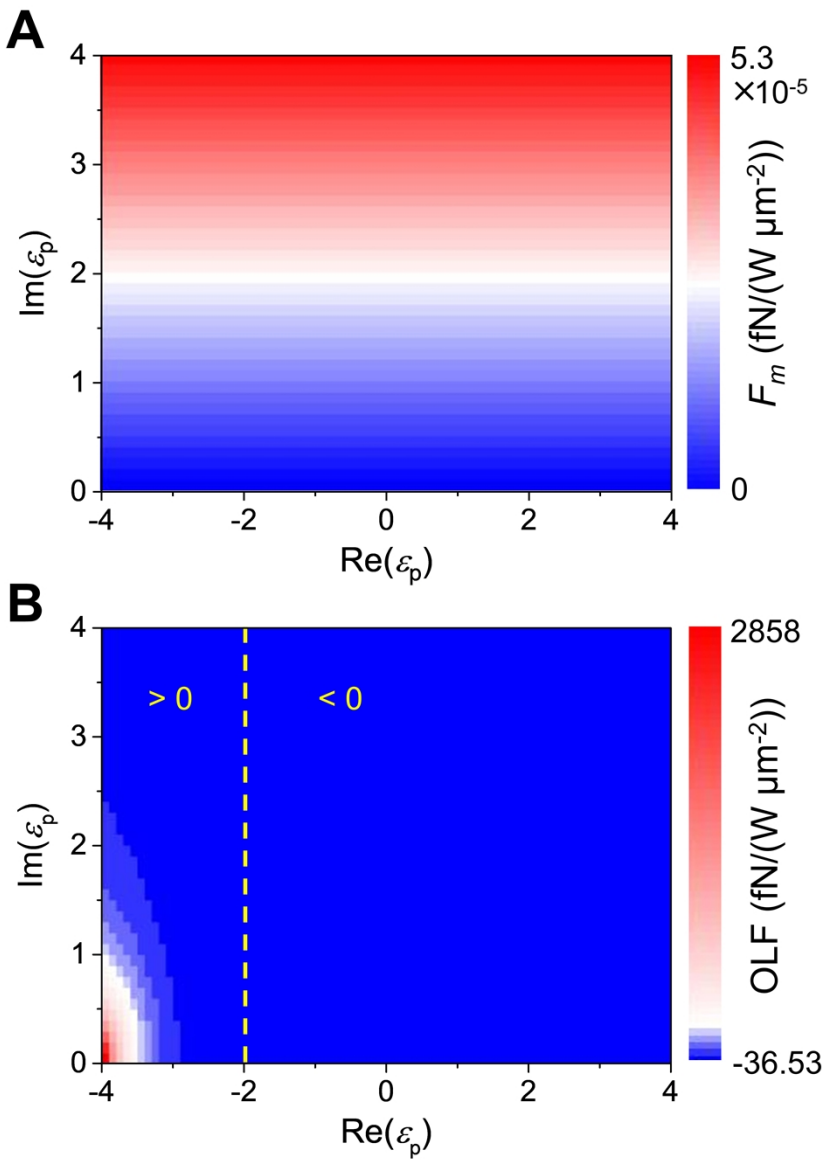

Fig. S13. Comparison of different contributions to the optical lateral force for different permittivities of the particle. a, The magnetic dipole contribution induced by $\mathbf{p}_O^m$. **b**, Optical lateral force calculated from equation (3). The magnetic dipole contribution (**a**) is much smaller than the total OLF (**b**) dominated by the force due to the electric-magnetic dipole coupling. The OLF changes from negative to positive when the real part of the particle permittivity $\mathrm{Re}\left(\varepsilon_p\right) < -2$. The OLF is also drastically enhanced when $\mathrm{Re}\left(\varepsilon_p\right)$ is negative and $\mathrm{Im}\left(\varepsilon_p\right) \to 0$. The simulation parameters are $w_x = 15$ μm, $w_y = 500$ μm, particle position $(x, y) = (400\text{ nm}, 0)$, $a = 25$ nm, $\varepsilon = 1.46^2$, $\mu = \mu_\mathrm{p} = 1$ and $\theta = 45°$. The OLFs are calculated by normalizing the intensity at $(x = 0, y = 0)$ to 1 W/μm^2, where it is highest.

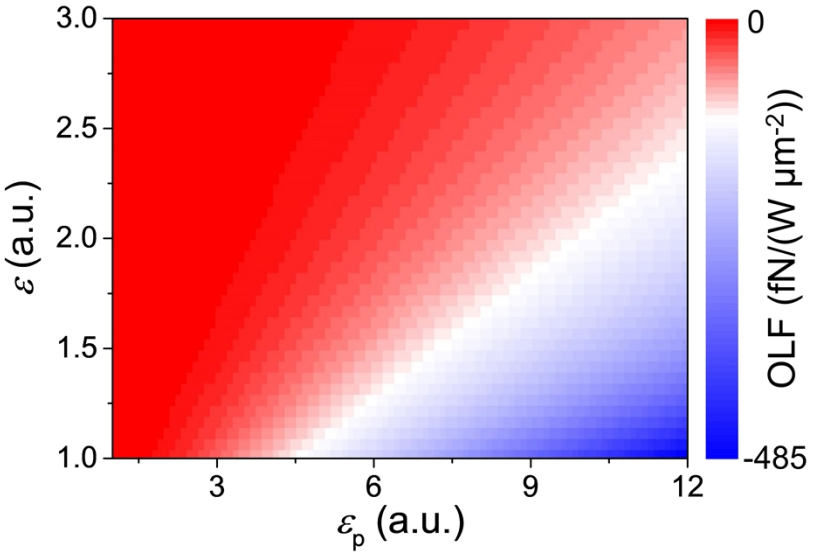

Fig. S14. Optical lateral force versus the permittivity of the medium ε and the particle ε_p. In sharp contrast to the optical gradient force, which is respectively an attractive or repulsive force when the permittivity of the particle is larger or smaller than that of the medium, the OLF remains positive in the whole map. The simulation parameters are w_x = 15 μm, w_y = 500 μm, particle position (x, y) = (400 nm, 0), a = 25 nm, $\mathrm{Im}(\varepsilon_p) = \mathrm{Im}(\varepsilon) = 0$, $\mu = \mu_p = 1$ and $\theta = 45°$. The OLFs are calculated by normalizing the intensity at (x = 0, y = 0) to 1 W/μm^2. The highest light intensity is reached at (x = 0, y = 0).

Supplementary Table S1: Ubiquitous SAM force in various systems

Configurations	Dominant force and predictable SAM forces	References
Evanescence waves	Gradient force in vertical SAM lateral force (observable)	15 (theory: force) 32, 62 (theory: force) 44 (experiment: force)
Highly focused single beams	Gradient force & SOI orbital force SAM lateral force (unobservable/transient)	30 (experiment: force) 34 (experiment: configuration) 36 (experiment: force)
Structured waves (Standing waves, structured guided waves, vortex beams, etc.)	Gradient force & SOI orbital force SAM lateral force (unobservable/transient)	35 (theory: force) 31 (experiment: force) 37 (experiment: configuration) 46 (experiment: configuration)
Unpolarized beam	Gradient force SAM lateral force (unobservable/transient)	47 (experiment: configuration)
Loosely focused line-shaped beam	Gradient force in the *x*-direction SAM lateral force in the *y*-direction (observable)	This work: force

Note:

The evanescence waves attract the particle onto the surface, and the SAM lateral force moves the particle laterally. This system is suitable for investigating the SAM lateral force, but is difficult to implement. The divergence of the incident beam for exciting evanescence waves may generate an extra optical gradient force which may overwhelm the SAM lateral force. Besides, the multiple scattering of light at the particle near the interface of the substrate and medium may also potentially affect the observation of the SAM lateral force.

Highly focused single beams generate a strong optical gradient force to attract the particle to the beam center, where no SAM lateral force exists due to the symmetry. The spin-orbit interactions (SOIs) generate a strong orbital force to interfere with the observation of the SAM lateral force.

Similarly, structured waves (such as standing waves, guided waves, and vortex beams) generate either strong intensity/phase-induced gradient forces or SOI-induced forces which may prevent the observation of the SAM lateral force.

The unpolarized beam also generates a strong gradient force, imposing a difficulty in observing the SAM lateral force.

In this work, the loosely focused line-shaped beam results in only the weak gradient force in the *y*-direction to facilitate the observation of the SAM-inhomogeneity-dependent lateral force in that direction. Meanwhile, the SOI effect is largely reduced by the loosely focused beam which is the main interference factor in highly focused beams, see the discussion in the main text.

In summary, any beam possessing a SAM will give rise to a SAM-inhomogeneity-dependent optical force when the beam has an electric or magnetic gradient that induces a spin momentum [equation (1)]. This particular force is parallel to the spin momentum vector. In most typical scenarios, the SAM-inhomogeneity-dependent force only considers the electric spin momentum $\mathbf{p}_s^e$ on an electric dipole, which is usually very weak (and overlooked), and can be easily overwhelmed by other dominant optical forces, such as the gradient force, SOI-induced force, etc. Therefore, one needs an appropriately devised system to rule out those dominant forces to facilitate the observation of the SAM-inhomogeneity-dependent lateral force.